Chemical Science

ROYAL SOCIETY OF CHEMISTRY

EDGE ARTICLE

View Article Online
View Journal | View Issue



Cite this: *Chem. Sci.*, 2026, **17**, 3516

All publication charges for this article have been paid for by the Royal Society of Chemistry

Received 28th October 2025
Accepted 16th December 2025

DOI: 10.1039/d5sc08329j

rsc.li/chemical-science

# Water-mediated kinetic engineering of CTF QDs for emerging solar cells

Manying Liu, *[a] Zikang Lei,[a] Peiyuan Ma,[a] Lixin Feng,[a] Yuanhao Wang,[a] Dandan Zhao,[a] Yanru Guo,[a] Yange Zhang,[a] Xin Zhao *[b] and Zhi Zheng *[a]

Covalent triazine framework quantum dots (CTF QDs) are promising low-toxicity, high-performance optoelectronic materials featuring molecular-level structural tunability and good charge-carrier mobility. Yet, achieving CTF QDs has long been hindered by the inherently rapid kinetics of triazine cyclization. Here, we overcome this limitation with a simple water-mediated kinetic strategy that modulates the forward Schiff-base reaction rate, thereby delaying triazine cyclization and controlling the degree of amidine–aldehyde polymerization. This approach produces CTF QDs smaller than 3 nm (denoted CTF-QD-1 and CTF-QD-2). By leveraging the pyridinic nitrogen and carbonyl oxygen-functionalized surface of CTF-QD-1 to coordinate interfacial $Pb^{2+}$ in $CsPbBr_3$ perovskites, we achieve effective defect passivation and controlled crystallization, enhancing the power conversion efficiency from 8.40% to 11.01%—a 31% relative improvement. This efficiency represents one of the highest values reported to date for all-inorganic $CsPbBr_3$ solar cells. This kinetic engineering paradigm addresses the long-standing challenge in synthesizing CTF QDs and unlocks their potential for high-efficiency photovoltaics.

## Introduction

Quantum dots (QDs) have long been investigated for their quantum-confinement effect and size-tunable photoluminescence, enabling widespread applications in the field of optoelectronics.[1,2] Major categories of QDs encompass the following: traditional cadmium- or lead-based QDs,[1,3] as well as perovskite QDs,[4,5] which offer high performance but pose toxicity concerns; heavy-metal-free alternatives such as InP and ZnSe,[6] which are more environmentally friendly but suffer from lower stability; epitaxially grown QDs,[7] often employed in single-photon sources; and carbon quantum dots (CQDs) known for low toxicity and biocompatibility but typically exhibiting inferior charge-carrier mobility.[8–11] Future development focuses on creating non-toxic, highly stable new materials and expanding their applications in sustainable technologies.

Covalent triazine frameworks (CTFs) are emerging as a class of crystalline organic semiconductors with precisely designable, tunable, and resolvable conjugated structures.[12–20] To date, research on CTF synthesis has predominantly focused on achieving high crystallinity and large crystal size, while studies concerning small-particle-size dispersion, processability, and especially their potential optoelectronic device applications have been largely overlooked.[21–23] Reducing CTFs to quantum-dot dimensions allows for molecular-level structural engineering, which promises good charge-carrier mobility, excellent dispersibility and processability, and enhanced optoelectronic performance. Consequently, the development of rational synthetic routes for CTF QDs opens new avenues for designing low-toxicity, high-performance photoelectric materials. However, the synthesis of CTF QDs remains a challenge, primarily due to the intrinsically rapid kinetics of triazine ring formation, which leads to uncontrolled polymerization, severe cross-linking, and consequently, great difficulty in controlling the particle size.[23–39] So far, only a few studies have been reported for the fabrication of CTF nanomaterials. They resorted to top–down exfoliation of bulk CTFs *via* oxidative $H_2O_2$/acid treatments[40–42] or small-molecule intercalation[43] to improve dispersion and processability. However, since their lateral dimensions (>10 nm) far exceed the typical quantum-confined size of QDs (generally <10 nm), these materials are more appropriately classified as nanosheets rather than CTF QDs.

In this context, if CTFs could be engineered into well-dispersed, colloidally stable quantum dots (CTF QDs), they would combine the advantages of molecular precision, rich surface coordination sites, and solution processability. Such CTF QDs could serve as ideal interfacial modifiers in thin-film inorganic solar cells, where they could uniformly passivate grain boundaries and defects, thereby enhancing both device efficiency and operational stability.[44–49] In this work, we developed a strategy to synthesize CTF QDs by controlling the reaction

[a]*Key Laboratory of Micro-Nano Materials for Energy Storage and Conversion of Henan Province, Institute of Surface Micro and Nano Materials, College of Chemical and Materials Engineering, Xuchang University, Henan 461000, China. E-mail: manyingliu988@xcu.edu.cn; zzheng@xcu.edu.cn*

[b]*State Key Laboratory of Organometallic Chemistry, Shanghai Institute of Organic Chemistry, Chinese Academy of Sciences, Shanghai 200032, China. E-mail: xzhao@sioc.ac.cn*

kinetics through a simple water-mediated polycondensation process. Through kinetic modulation, we successfully achieved CTF-QD-1 and CTF-QD-2 with sizes below 3 nm. Using $CsPbBr_3$ as a test platform, we incorporated CTF-QD-1 into $CsPbBr_3$ solar cells, achieving a 31% PCE increase (from 8.40% to 11.01%). This efficiency ranks among the highest reported for inorganic devices of this class. Our work pioneers a kinetic engineering approach for CTF quantum dots and unlocks their potential in photovoltaic devices for the first time.

## Results and discussion

The CTF QDs were synthesized *via* a bottom-up, kinetically controlled microwave-assisted approach using water to regulate the polymerization in condensation reactions (details in the Experimental section, SI). During the preparation process (Fig. 1a), water was introduced into the amidine–aldehyde condensation polymerization system to modulate the kinetics of the forward Schiff-base reaction. The Schiff-base reaction between amidine and aldehyde monomers is reversible. In the absence of water modulation, the reaction proceeds rapidly, generating abundant Schiff-base intermediates that quickly undergo triazine cyclization. This leads to uncontrolled polymerization and the formation of large particles. In the presence of water, the equilibrium of the Schiff-base reaction shifts, reducing the concentration of Schiff-base intermediates. This control subsequently delays triazine cyclization and limits structural expansion, enabling precise control over the amidine–aldehyde polymerization degree. This intervention facilitates rapid generation of crystalline nuclei, suppresses Ostwald

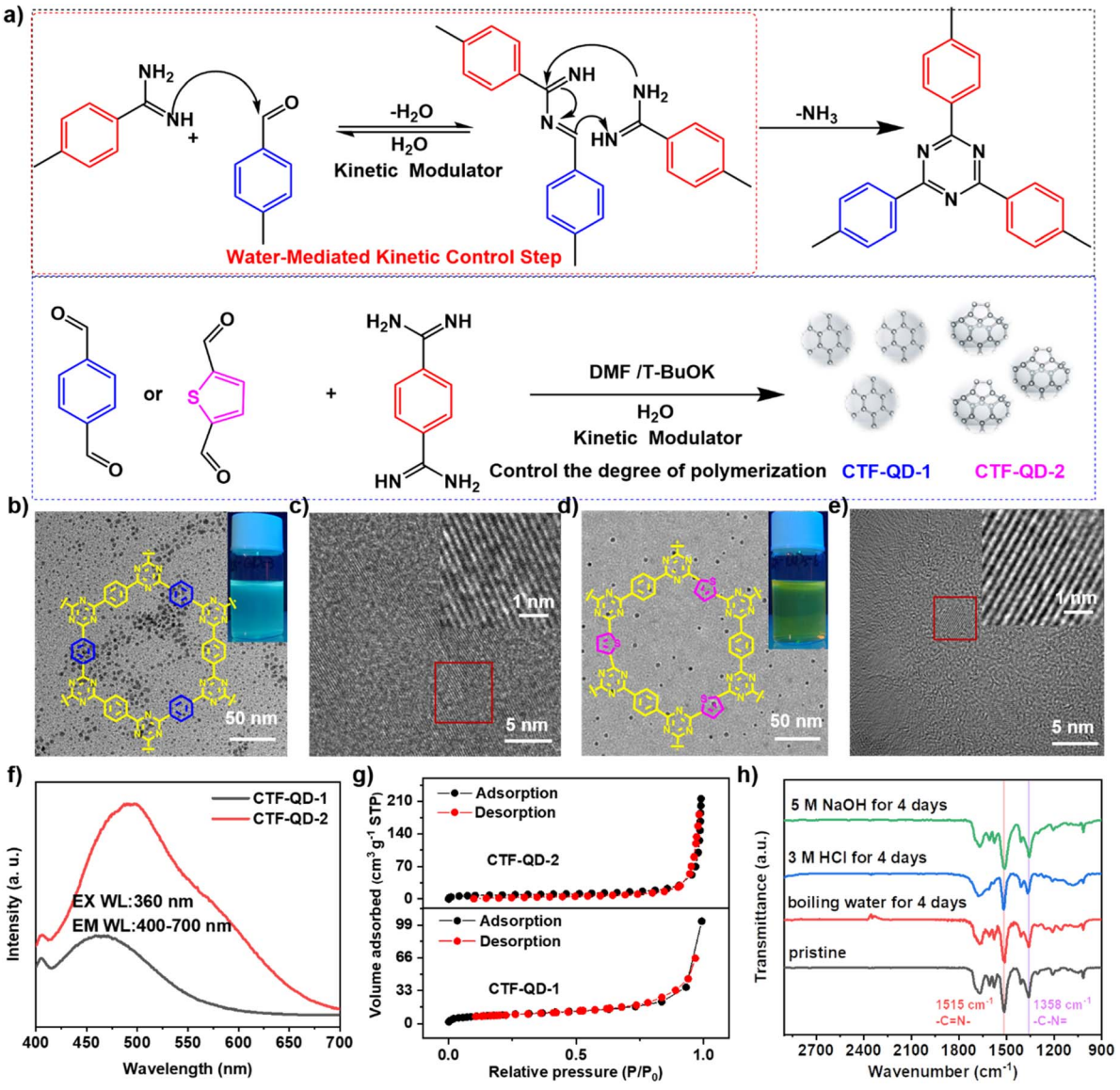


Fig. 1 (a) Schematic diagram of the synthesis of CTF QDs *via* water-mediated kinetic control of the degree of polymerization. TEM images of CTF-QD-1 (b) and CTF-QD-2 (d), respectively (insets: optical images and structural schematics of the CTF QDs). HR-TEM images of CTF-QD-1 (c) and CTF-QD-2 (e), respectively. (f) PL spectra of CTF QDs. (g) $N_2$ adsorption (black) and desorption (red) isotherms (77 K) of CTF QDs. (h) FT-IR spectra of CTF-QD-1 under various conditions.

ripening and promotes formation of CTF QDs. Transmission electron microscopy (TEM) was employed to examine the morphology of CTF QDs. As shown in Fig. 1b, CTF-QD-1 is uniformly distributed with an average particle size of approximately 2.6 nm and exhibits blue fluorescence. In Fig. 1d, CTF-QD-2 displays uniform distribution with an average particle size of approximately 2.4 nm and emits green fluorescence. Fig. 1f further illustrates that the green fluorescence intensity of CTF-QD-2 at 505 nm is stronger than the blue fluorescence intensity of CTF-QD-1 at 475 nm. High-resolution TEM (HR-TEM) images (Fig. 1c and e) reveal clear lattice fringes for both CTF-QD-1 and CTF-QD-2, indicating their short-range ordered structure.

The adsorption–desorption curves of $N_2$ (recorded at 77 K) for CTF-QD-1 and CTF-QD-2 display a type III pattern (as shown in Fig. 1g). These curves do not exhibit a clear turning point at low relative pressures ($P/P_0$). Brunauer–Emmett–Teller (BET) analysis graphs reveal that CTF-QD-1 has a specific surface area of 29 $m^2\ g^{-1}$, while for CTF-QD-2 it is 33 $m^2\ g^{-1}$ (Fig. S1). Therefore, this specific surface area is primarily attributed to the macropores formed by stacking. Thermogravimetric analysis (Fig. S2) evaluated the thermal stability of CTF QDs. Both CTF-QD-1 and CTF-QD-2 exhibited less than 5 wt% weight loss up to 260 °C. As the temperature increased, CTF-QD-2 demonstrated slightly better thermal stability than CTF-QD-1. Powder X-ray diffraction (PXRD) patterns of CTF QDs (Fig. S3) indicate the absence of long-range order. Using a water-modulated microwave-assisted method, we successfully synthesized CTF QDs with particle sizes below 3 nm and exhibiting tunable fluorescence color, as well as good thermal stability.

Fourier transform infrared (FT-IR) spectroscopy provided detailed structural elucidation of the synthesized materials. As illustrated in Fig. 2a, characteristic vibrational signatures at 1516 $cm^{-1}$ (C=N stretching) and 1344 $cm^{-1}$ (C–N stretching) confirm successful triazine ring formation.[24] Additional diagnostic peaks at 3383 $cm^{-1}$ (O–H stretching), 1660 $cm^{-1}$ (C=O stretching), and 1215 $cm^{-1}$ (C–O stretching) suggest incomplete polycondensation with residual aldehyde functionalities (–CHO groups). After exposure to strong alkali (5 M NaOH), strong acid (3 M HCl), and boiling water for four days, the FT-IR spectra of CTF QDs showed no changes (Fig. 1h), demonstrating their excellent chemical stability. Solid-state cross-polarization magic angle spinning $^{13}C$ nuclear magnetic resonance (CP-MAS $^{13}C$-NMR) further elucidated the structure of CTF QDs. The spectrum for CTF-QD-1 (Fig. 2b) displays chemical shifts at 127.6 ppm, 138.2 ppm, and 169.1 ppm assigned to phenyl and triazine carbons, with an additional peak at 195.6 ppm attributed to the carbonyl carbon of the residual aldehyde.[50] For CTF-QD-2, peaks at 139.2 ppm, 137.1 ppm, 128.1 ppm, and 169.7 ppm correspond to thiophene ring carbons and triazine carbons, with a peak at 195.6 ppm indicating residual aldehyde. FT-IR and solid-state $^{13}C$ NMR spectroscopy confirmed the formation of triazine rings in CTF QDs, and revealed some residual aldehyde functionalities, which demonstrate excellent chemical stability even after harsh treatments.

To support the structural analysis, X-ray photoelectron spectroscopy (XPS) analysis was performed on CTF-QD-1 and CTF-QD-2 to determine their elemental compositions. The survey spectra revealed peaks for C 1s, N 1s, and O 1s in both samples, with additional S 2p peaks in CTF-QD-2 (Fig. 2c). These results agree with the elemental analysis data (Table S1), corroborating the compositional differences between the two materials. The N 1s core-level spectrum displayed peaks at 399.3 eV and 400.4 eV, assigned to nitrogen atoms within

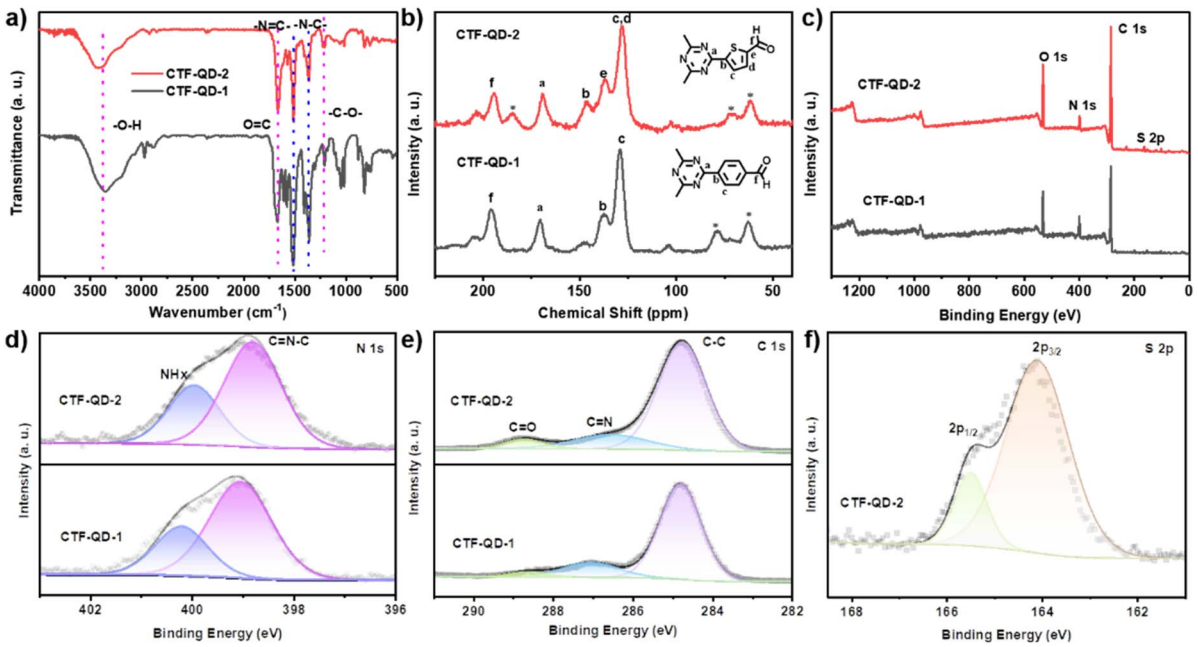


Fig. 2 (a) FT-IR and (b) CP-MAS $^{13}C$-NMR spectra of CTF-QD-1 and CTF-QD-2. In the $^{13}C$ NMR spectrum with a magic angle spinning rate of 12 kHz and sidebands preserved, the right-hand sideband is marked with an asterisk (*). (c) XPS full spectra, (d) N1s spectra, and (e) C1s spectra of CTF-QD-1 and CTF-QD-2, as well as (f) the S2p spectrum of CTF-QD-2.

triazine linkages (Fig. 2d).[51,52] The C 1s core-level spectrum was deconvoluted into three components with binding energies of 284.7 eV (C–C), 286.8 eV (C=N), and 288.7 eV (C=O) (Fig. 2e).[53] The S 2p core-level spectrum of CTF-QD-2 was fitted to S $2p_{3/2}$ and S $2p_{1/2}$ peaks at 164.1 eV and 165.5 eV, confirming the presence of sulfur (Fig. 2f). These results confirm that CTF-QD-1 and CTF-QD-2 are composed of CTF fragments with incompletely reacted aldehyde groups.

To elucidate the formation mechanism of CTF QDs *via* a kinetically controlled microwave-assisted approach, we investigated the size, specific surface area, and nitrogen adsorption–desorption properties of CTF-QD-1 synthesized using different amounts of water. The initial reaction between the amidine and aldehyde is a Schiff base reaction that occurs under basic conditions.[38] This is a reversible process that produces water as a byproduct. By introducing additional water into the system, the dynamic equilibrium can be manipulated to suppress the forward reaction progression, thereby controlling the degree of polymerization and facilitating the formation of small molecular fragments of CTFs. As illustrated in Fig. S4, the solution becomes progressively clearer with the addition of water, as evidenced by the Tyndall effect, suggesting a gradual reduction in particle size. TEM image analysis shows that the morphology and particle size of CTF-QDs exhibit significant changes with increasing water content in the synthesis system (0–4 mL). Specifically: (1) without added water (0 mL), the synthesized CTF-QD-1 exhibits larger particle sizes and poor dispersion (Fig. S5); (2) after adding water (1–4 mL), the resulting products consist of well-dispersed nanoparticles; (3) as the water content increases from 1 mL to 4 mL, the average size of CTF-QDs decreases (Fig. 3a–d). The average particle sizes for different water contents are 39.91 nm (1 mL), 3.41 nm (2 mL), 2.64 nm (3 mL), and 2.30 nm (4 mL), as shown in Fig. 3e and S6. Notably, the most significant size reduction occurs when 2 mL of water is added, representing a critical inflection point. Beyond this point, further increases in water content result in minimal changes in particle size; however, the CTF-QD yield notably drops when the water dosage is increased from 3 mL (yield: 27.6%) to 4 mL (yield: 10.1%). This yield decline arises because excess water (≥4 mL) excessively suppresses the amidine–aldehyde condensation reaction: water shifts the equilibrium of the reversible Schiff-base reaction far toward reactants, reducing the concentration of Schiff-base intermediates to levels insufficient for efficient triazine cyclization and nucleation. As a result, fewer CTF QD nuclei form, and unreacted monomers remain in the solution, leading to a sharp decrease in QD yield. These findings demonstrate that the kinetically controlled synthesis of CTF-QDs can be precisely tuned through water-mediated equilibrium manipulation of the reversible Schiff-base reaction.

The $N_2$ adsorption–desorption isotherms (measured at 77 K) of CTF QDs synthesized with different amounts of water exhibit type III behavior (Fig. 3f) with no distinct inflection point at low relative pressures ($P/P_0$). Thus, CTF QDs do not possess a well-developed microporous structure; instead, they are fragments formed during CTF synthesis. BET analysis plots demonstrate the influence of water content on the specific surface area of CTF QDs synthesized with varying amounts of water (0 mL, 1 mL, 2 mL, 3 mL, and 4 mL) (Fig. 3g). The specific surface areas for these water contents are 88 $m^2 g^{-1}$, 40 $m^2 g^{-1}$, 36 $m^2 g^{-1}$, 32 $m^2 g^{-1}$, and 15 $m^2 g^{-1}$, respectively. As the amount of water increases, the specific surface area decreases progressively, confirming that

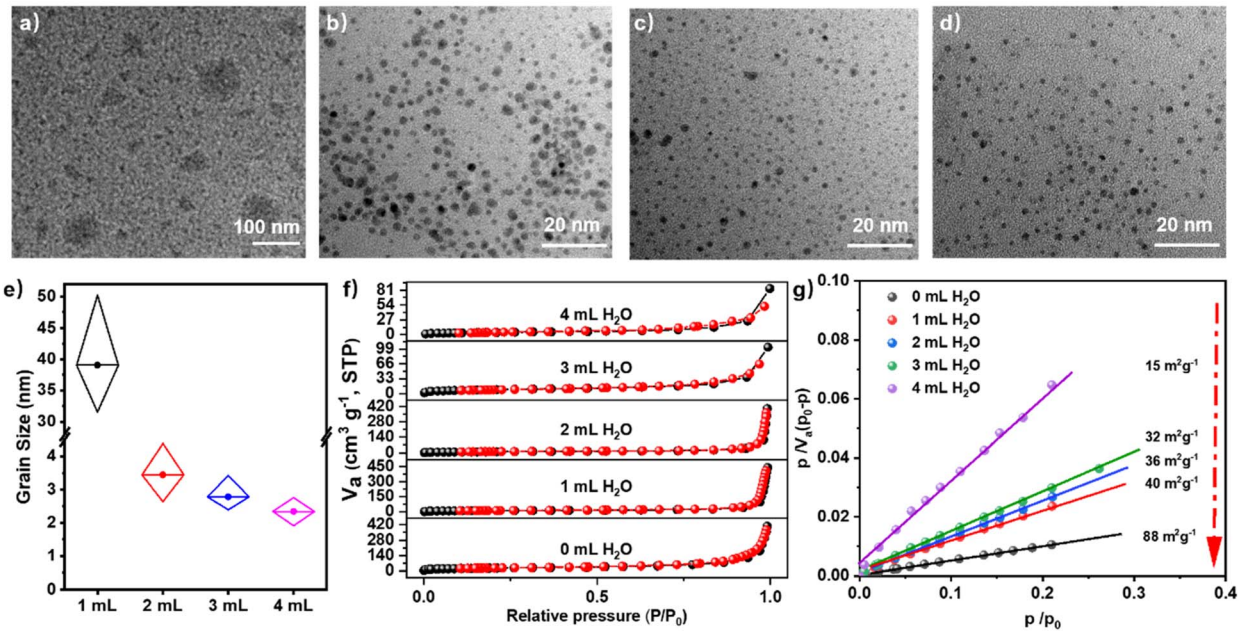


Fig. 3 TEM images of CTF-QD-1 obtained with the addition of (a) 1 mL, (b) 2 mL, (c) 3 mL, and (d) 4 mL water during the polymerization reaction. (e) Particle size distribution curves for CTF-QD-1 samples synthesized with 1 mL, 2 mL, 3 mL, and 4 mL water. (f) $N_2$ adsorption (black) and desorption (red) isotherms (77 K) of CTF-QD-1 samples prepared with different water amounts. (g) BET analysis plots of CTF-QD-1 samples prepared with different water amounts.

water plays a decisive role in determining both the specific surface area and particle size during the amidine–aldehyde condensation polymerization reaction. The amidine–aldehyde condensation reaction involves Schiff base formation followed by a Michael addition.[38,54] Adding water during the Schiff base formation process significantly inhibits further polymerization, thereby facilitating the creation of CTF QDs instead of larger polymers. By leveraging water as a dynamic polymerization modulator, it is possible to precisely control the reaction kinetics during the amidine–aldehyde condensation polymerization process. As illustrated in Fig. S7, the C=O stretching vibration peak exhibits a progressive increase in intensity correlating to increased water content, suggesting incomplete conversion of aldehyde functional groups. Importantly, this deliberate retention of –CHO groups is not a synthetic artefact but a design feature: the carbonyl oxygen in –CHO serves as an additional Lewis base site, which later enables synergistic coordination with $Pb^{2+}$ in $CsPbBr_3$ perovskites. This controlled polymerization under aqueous conditions aids in the formation of quantum dots. Therefore, CTF QDs are essentially small fragments formed during CTF synthesis.

In this work, we selected CTF-QD-1 over CTF-QD-2 for its structural simplicity. CTF-QD-1 contains only the characteristic functional groups of covalent triazine frameworks (pyridinic nitrogen and carbonyl oxygen), while CTF-QD-2 incorporates additional sulfur atoms from thiophene moieties. This simpler structure allows us to specifically investigate how dimensional reduction of CTFs affects $CsPbBr_3$ solar cell performance, without confounding effects from extraneous heteroatoms. The preparation of $CsPbBr_3$ films typically involves a multi-step spin-coating method due to the solubility limit of bromide ions (see the Experimental section for details). The CTF-QD-1-incorporating $CsPbBr_3$ ($CsPbBr_3$@CTF-QD-1) film was utilized as an absorber material to fabricate all-inorganic solar cells. Fig. 4a illustrates the device architecture of the all-inorganic solar cells with the structure FTO/compact $SnO_2$/$CsPbBr_3$@CTF-QD-1/carbon. The *J–V* curves for $CsPbBr_3$@CTF-QD-1 (2.0 mg $L^{-1}$) and pure $CsPbBr_3$ solar cells are displayed in Fig. 4b, while additional *J–V* plots for $CsPbBr_3$@ CTF-QD-1 at various CTF-QD-1 concentrations can be found in Fig. S8. Table S2 provides a summary of the photovoltaic parameters for $CsPbBr_3$ solar cells at different CTF-QD-1 concentrations. The $CsPbBr_3$@CTF-QD-1 (2.0 mg $L^{-1}$) solar cell demonstrates significantly improved performance compared to pristine $CsPbBr_3$ devices.

While the control device exhibited a PCE of 8.40% ($J_{sc}$ = 7.96 mA $cm^{-2}$, $V_{oc}$ = 1.55 V, FF = 68.30%), the CTF-QD-1 modified device achieved an impressive 11.01% efficiency ($J_{sc}$ = 9.49 mA $cm^{-2}$, $V_{oc}$ = 1.56 V, FF = 74.57%), representing a 31% enhancement and approaching the reported maximum of 11.21% (Table S4).[44] This performance gain notably surpasses the 15% improvement previously achieved by bulk ECTF-1 modified $CsPbBr_3$@ECTF-1, despite their structural similarities.[43] The superior performance of CTF-QD-1 over ECTF-1 can be attributed to its unique nanoscale characteristics: (1) smaller particle size, which enhances dispersibility, and (2) higher density of active sites, which facilitates effective defect passivation at the interface.

To systematically evaluate the influence of CTF-QD-1 on the photovoltaic performance of $CsPbBr_3$ solar cells, a comprehensive statistical analysis was conducted on 24 solar cells. This analysis focused on key parameters, including PCE, $J_{sc}$, $V_{oc}$, and FF (as illustrated in Fig. 4c). The results revealed that FF, $J_{sc}$, and PCE exhibited a concentration-dependent trend of initial increase followed by decrease, as presented in the boxplots with

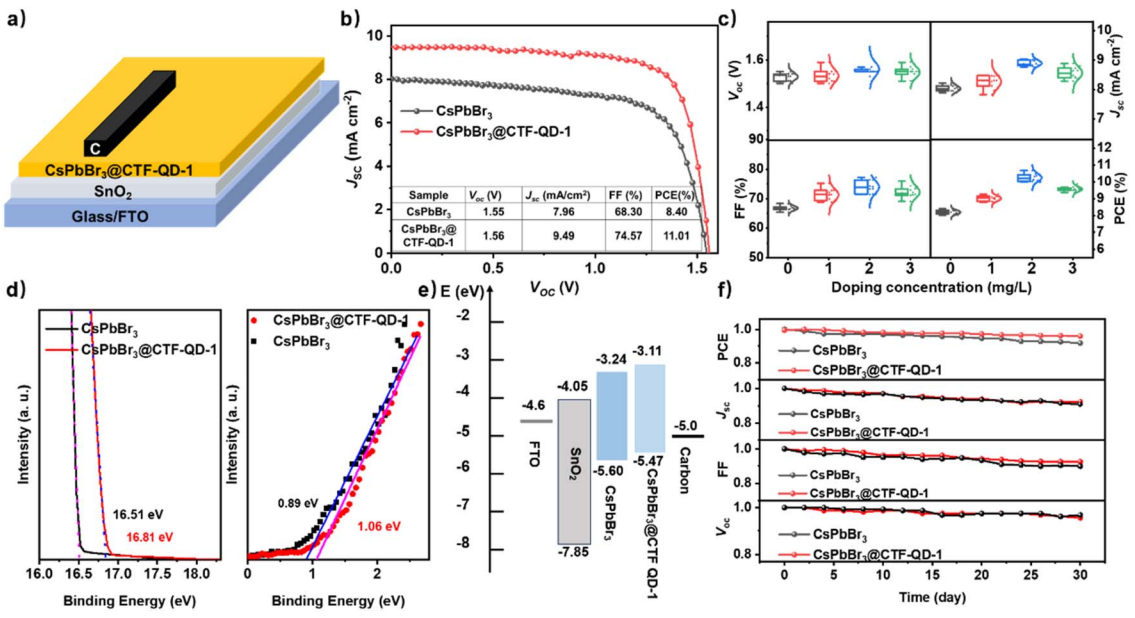


Fig. 4 (a) Device configuration of $CsPbBr_3$@CTF QD based solar cells. (b) *J–V* curves of $CsPbBr_3$ and $CsPbBr_3$@CTF-QD-1. (c) PV parameters ($J_{sc}$, $V_{oc}$, FF, PCE) for $CsPbBr_3$ solar cells with varying CTF-QD-1 concentrations. (d) UPS spectra of the $CsPbBr_3$ and $CsPbBr_3$@CTF-QD-1 films. (e) Energy gradient diagram for $CsPbBr_3$ and $CsPbBr_3$@CTF-QD-1 solar cells. (f) Long-term stability of PCE, $J_{sc}$, FF, and $V_{oc}$ under RH = 50%, $T$ = 25 °C conditions.

varying CTF-QD-1 concentrations. Meanwhile, $V_{oc}$ exhibited minimal variations across different concentrations, indicating negligible fluctuation. These observations highlight the substantial role of CTF-QD-1 incorporation in enhancing photovoltaic performance, primarily by influencing $J_{sc}$ and FF, which in turn significantly boosted the overall efficiency of the solar cells.

To elucidate the role of CTF-QD-1 doping in the energy-level structure and photovoltaic performance of $CsPbBr_3$ solar cells, ultraviolet photoelectron spectroscopy (UPS) was employed to probe the interfacial energetics of pristine $CsPbBr_3$ and $CsPbBr_3$@CTF-QD-1 films (Fig. 4d). UPS analysis revealed that CTF-QD-1 incorporation induces a systematic upward shift in the electronic bands: the conduction band minimum (CBM) rose from −3.24 eV to −3.11 eV, while the valence band maximum (VBM) increased from −5.60 eV to −5.47 eV (Fig. 4e). Critically, CTF-QD-1 doping elevates the Fermi level from −4.41 eV (pristine $CsPbBr_3$) to −4.71 eV ($CsPbBr_3$@CTF-QD-1). This Fermi level modulation, corroborated by electronic structure analysis (Fig. S9), drives the concomitant upshift of both the VBM and CBM. These CTF-QD-1-mediated energy-level modifications establish a built-in band alignment proximal to the $CsPbBr_3$/carbon interface. This optimized alignment facilitates interfacial charge separation and promotes hole transfer from the $CsPbBr_3$@CTF-QD-1 layer to the carbon electrode, thereby enhancing overall device performance.[55] External quantum efficiency (EQE) spectra (Fig. S10) confirm strong light absorption between 340 and 530 nm for both devices, consistent with UV-vis data. Stability assessments further underscore CTF-QD-1's role: after 30 days of ambient exposure (unencapsulated), the $CsPbBr_3$@CTF-QD-1 device exhibited a minimal PCE degradation of ∼3.7%, significantly outperforming the 8.9% loss observed for pristine $CsPbBr_3$ (Fig. 4f). This demonstrates that CTF-QD-1 doping substantially enhances the operational stability of $CsPbBr_3$ photovoltaics.

The obtained CTF-QD-1 quantum dots can induce the crystal growth of $CsPbBr_3$ and facilitate high-quality crystalline $CsPbBr_3$@CTF-QD-1 films *via* synergistic coordination between pyridinic N and carbonyl O (from –CHO groups) with $Pb^{2+}$.[43] As shown in Fig. S11, the XRD peaks at 15.3°, 21.8°, 26.6°, 30.8°, and 37.9° correspond to the (100), (110), (111), (200), and (211) planes of $CsPbBr_3$ (JCPDS No. 54-0752).[56] Additional peaks at 11.8° and 29.5° suggest the presence of the $CsPb_2Br_5$ phase.[57] The addition of CTF-QD-1 enhanced XRD intensities while keeping peak positions and numbers unchanged, suggesting no alteration in structure or composition. As depicted in the SEM images (Fig. S12), the average particle size of $CsPbBr_3$ initially increases from 0.8 μm to 1.2 μm and subsequently decreases to 1.0 μm with the increasing concentration of added CTF-QD-1. This trend suggests that the –CHO– derived O and pyridinic N in CTF-QD-1 quantum dots suppress excessive nucleation and promote grain growth, yielding denser films with fewer grain boundaries. FT-IR and XPS analyses corroborate the coordination-driven film formation mechanism. The $PbBr_2$@-CTF-QD-1 complex exhibits characteristic blue shifts of 16 $cm^{-1}$ (C═O), 5 $cm^{-1}$ (C–N) and 8 $cm^{-1}$ (C═N) in FT-IR spectra relative to pristine CTF-QD-1 (Fig. S13), indicating reduced electron density on the CTF-QD-1 surface due to simultaneous coordination of pyridinic N and –CHO derived O with $Pb^{2+}$ ions (dual Lewis base–Lewis acid interactions). This interaction is further confirmed by XPS studies: N 1s spectra verify the presence of pyridinic N in $CsPbBr_3$@CTF-QD-1 composites (Fig. S14 and S15), while a 0.15 eV binding energy shift in Pb 4f peaks (Fig. S16) reflects the combined effect of N–Pb and O–Pb bond formation (from –CHO groups). The synergistic coordination

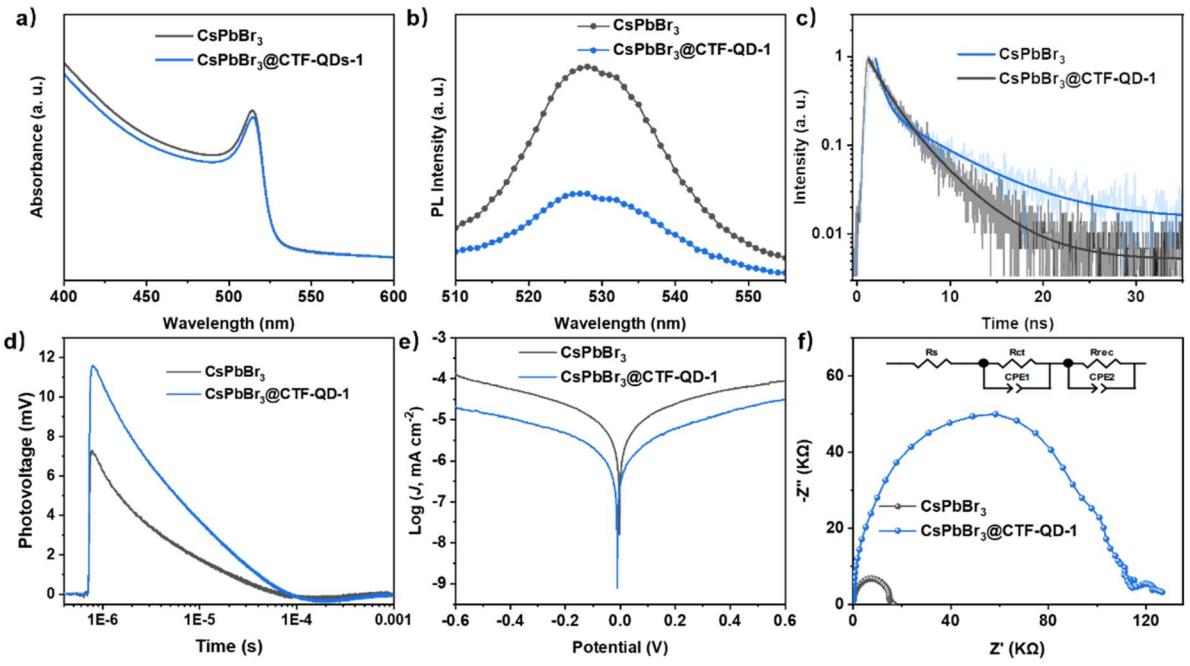


Fig. 5 (a) Absorbance spectra, (b) steady-state PL spectra, (c)TRPL spectra, and (d) TSPV spectra of $CsPbBr_3$ and $CsPbBr_3$@CTF-QD-1 films. (e) *J*–*V* curves in the dark and (f) Nyquist plot curves based on $CsPbBr_3$ and $CsPbBr_3$@CTF-QD-1 devices.

effect facilitates $CsPbBr_3$ crystal growth, yielding high-quality crystalline films essential for enhanced photovoltaic performance. This optimized structure and interfacial interaction directly translate into improved optoelectronic properties, as revealed by the following spectroscopic and electrical characterization.

As indicated by the UV-vis absorption spectra (Fig. 5a), the absorption edge of the $CsPbBr_3$@CTF-QD-1 film remained unchanged compared to that of the reference $CsPbBr_3$. However, the steady-state photoluminescence intensity (PL) of the $CsPbBr_3$@CTF-QD-1 film was reduced relative to $CsPbBr_3$, suggesting a decrease in defects and a suppression of photogenerated charge recombination (Fig. 5b). Time-resolved photoluminescence (TRPL) spectra were employed using a bi-exponential decay model to investigate the carrier lifetime of the $CsPbBr_3$@CTF-QD-1 film.[57] The average carrier lifetime was prolonged from 2.89 ns for pristine $CsPbBr_3$ to 2.99 ns for $CsPbBr_3$@CTF-QD-1 (Fig. 5c). This increase suggests enhanced electron extraction and transfer within the $CsPbBr_3$@CTF-QD-1 films compared with those within the pristine $CsPbBr_3$ films. Transient surface photovoltage (TSPV) techniques were utilized to analyze the photo-induced charge behavior of photovoltaic thin films, enabling a rapid assessment and prediction of their photovoltaic properties.[58–60] The TSPV measurements show that the photovoltage magnitude for the $CsPbBr_3$@CTF-QD-1 film is greater than that of the unmodified $CsPbBr_3$ film, indicating an enhancement in charge separation efficiency (Fig. 5d). Based on prior research,[59,61,62] the parameter $L = \tau_t/\tau_r$ has been employed to gauge the photoelectric performance of perovskite materials, where $\tau_t$ denotes the time from photovoltage initiation to its peak value, while $\tau_r$ signifies the duration from the peak to complete recombination of the photo-generated charge carriers. A lower $L$ value typically indicates a more efficient and faster carrier transfer process. The measured $\tau_t$, $\tau_r$, and $L$ values are summarized in Table S3. Specifically, the $L$ value for the $CsPbBr_3$@CTF-QD-1 film ($1.16 \times 10^{-2}$) is significantly lower than that of the pristine $CsPbBr_3$ film ($3.14 \times 10^{-2}$), suggesting that CTF-QD-1 facilitates photoinduced carrier transfer, likely through its inductive effect on crystal growth *via* pyridinic N–$Pb^{2+}$ coordination interactions.

Additionally, Nyquist plots were utilized to elucidate the charge transport kinetics in perovskite solar cells (Fig. 5f). The inset depicts the equivalent circuit model employed for impedance analysis of these solar cells. The semicircular arc corresponds to the charge recombination resistance of the device. Relative to the pristine $CsPbBr_3$ device, the $CsPbBr_3$@-CTF-QD-1 device exhibits a higher charge recombination resistance, facilitating more efficient charge separation and transfer with minimal recombination. This enhancement is primarily attributed to the improved quality of the $CsPbBr_3$ film, characterized by a reduced density of trap states. Fig. 5e shows the dark $J$–$V$ characteristics of $CsPbBr_3$ and $CsPbBr_3$@CTF-QD-1 devices. Upon incorporation of CTF-QD-1, the $CsPbBr_3$@CTF-QD-1 devices show a markedly lower dark-current density than the control $CsPbBr_3$ cells, which indicates that CTF-QD-1 facilitates the extraction of photogenerated carriers and thereby suppresses carrier recombination. Thus, the $CsPbBr_3$ film modified with CTF-QD-1 demonstrates superior film quality, characterized by fewer defects, which effectively enhances the separation and transfer of photogenerated charges.

Collectively, the remarkable enhancement in $CsPbBr_3$ solar cell performance upon incorporating CTF-QDs is directly governed by its unique molecular structure, which enables multifunctional interfacial modulation. The key structural features of CTF-QDs—namely, their pyridinic nitrogen-rich triazine framework and residual aldehyde groups—are pivotal for its properties. These functional sites act as strong Lewis bases, effectively coordinating with under-coordinated $Pb^{2+}$ ions at the perovskite surface and grain boundaries. This coordination achieves two critical functions simultaneously: it provides excellent defect passivation, suppressing non-radiative recombination, and it modulates the crystallization kinetics of $CsPbBr_3$, leading to the formation of larger, high-quality grains. Consequently, this synergistic action results in enhanced charge carrier lifetime, improved charge extraction, and significantly reduced trap-assisted recombination. This structure-driven interfacial optimization directly boosts photovoltaic parameters ($J_{sc}$, FF, and PCE).

## Conclusions

In summary, we have synthesized well-defined CTF-based quantum dots (CTF-QD-1 and CTF-QD-2) through a water-mediated kinetic strategy that controls amidine–aldehyde polymerization by modulating Schiff-base reaction kinetics. Synergistic $Pb^{2+}$ coordination by CTF-QD-1's pyridinic N and aldehyde groups enables both crystallization control and defect passivation in $CsPbBr_3$ solar cells, achieving a 31% efficiency gain (8.40% → 11.01%). Furthermore, stability tests reveal that CTF-QD-1 dramatically suppresses device degradation, reducing the PCE loss by more than half (from 8.9% to 3.7%) over 30 days compared to the control device. Based on the principle of water-regulated reversible reaction kinetics, the rational design and synthesis of functionalized CTF QDs can be achieved by selecting different amine/aldehyde monomers. This study not only resolves the synthetic challenge of producing size-tunable CTF QDs but also establishes their transformative potential as interfacial modifiers in high-performance and stable photovoltaics, offering a general kinetic engineering paradigm for the design of functional nanomaterials.

## Author contributions

M. Liu: supervision, methodology, data analysis and writing – original draft. Z. Lei: prepared CTF quantum dots and tested solar cell performance. P. Ma: infrared spectroscopy and electrochemical characterization. L. Feng: explored CTF QD preparation conditions. Y. Wang: reproduced CTF QDs, verified reproducibility. D. Zhao and Y. Guo: guided solar cell performance testing. Y. Zhang: guided solar cell device structure design. X. Zhao: conceptualization, review and editing. Z. Zheng: conceptualization, writing – review and editing, supervision, funding acquisition.

## Conflicts of interest

The authors declare no conflict of interest.

## Data availability

The data that support the findings of this study are available in the supplementary information (SI) of this article. Supplementary information: materials and methods; characterizations including BET, TG, XRD, FT-IR, and XPS data; XRD patterns of CTF-QD-1/2; digital photos and TEM images; an energy-level diagram; *J*–*V* and EQE curves; SEM images and statistical particle-size analyses; elemental composition tables; and photovoltaic and TSPV parameters. See DOI: https://doi.org/10.1039/d5sc08329j.

## Acknowledgements

This work was financially supported by the National Natural Science Foundation of China (Grant No. 52472255, 22309158); Science and Technology Project of Henan Province (252102230120); Higher Education and Teaching Reformation Project (2024SJGLX0451); Academic Degrees & Graduate Education Reform Project of Henan Province (YJS2022JD34); Key Research and Development Projects of Universities in Henan Province (23B430009); Natural Science Foundation of Henan Province (232300420099); Key Scientific Research Project of Higher Education in Henan Province (25A150036); and Scientific Research Project of Xuchang University (2025ZD005).

## Notes and references

1 F. P. García de Arquer, D. V. Talapin, V. I. Klimov, Y. Arakawa, M. Bayer and E. H. Sargent, *Science*, 2021, **373**, eaaz8541.
2 F. Yarur Villanueva, V. Quezada Novoa, P. Rusch, S. Toso, M. W. Terban, Y. P. Ivanov, J. C. Chu, M. J. Kirshenbaum, E. Nikbin, M. J. Gendron Romero, M. Prato, G. Divitini, J. Y. Howe, M. W. B. Wilson and L. Manna, *J. Am. Chem. Soc.*, 2025, **147**, 29413–29422.
3 S. Morozov, E. L. Pensa, A. H. Khan, A. Polovitsyn, E. Cortés, S. A. Maier, S. Vezzoli, I. Moreels and R. Sapienza, *Sci. Adv.*, 2020, **6**, eabb1821.
4 Q. Shan, Y. Dong, H. Xiang, D. Yan, T. Hu, B. Yuan, H. Zhu, Y. Wang and H. Zeng, *Adv. Funct. Mater.*, 2024, **34**, 2401284.
5 M. Leng, Y. Yang, K. Zeng, Z. Chen, Z. Tan, S. Li, J. Li, B. Xu, D. Li, M. P. Hautzinger, Y. Fu, T. Zhai, L. Xu, G. Niu, S. Jin and J. Tang, *Adv. Funct. Mater.*, 2017, **28**, 1704446.
6 L. Jin, G. S. Selopal, X. Tong, D. F. Perepichka, Z. M. Wang and F. Rosei, *Adv. Mater.*, 2024, **36**, 2402912.
7 H. Li, Q. Peng, X. Xu and J. Wang, *Adv. Photonics*, 2023, **5**, 060503.
8 L. Wang, W. Li, L. Yin, Y. Liu, H. Guo, J. Lai, Y. Han, G. Li, M. Li, J. Zhang, R. Vajtai, P. M. Ajayan and M. Wu, *Sci. Adv.*, 2020, **6**, eabb6772.
9 Z. Bian, E. Gomez, M. Gruebele, B. G. Levine, S. Link, A. Mehmood and S. Nie, *Chem. Sci.*, 2025, **16**, 4195–4212.
10 T. Yuan, G. Zhao, D. Tang, X. Song, J. Du, Z. Yu, Y. Zhang, L. Sui, X. Li, Y. Li, L. Shen, F. Yuan, W. Jiang and L. Fan, *J. Am. Chem. Soc.*, 2025, **147**, 28504–28512.
11 C. Xia, S. Zhu, T. Feng, M. Yang and B. Yang, *Adv. Sci.*, 2019, **6**, 1901316.
12 R. Sun, X. Yang, X. Hu, Y. Guo, Y. Zhang, C. Shu, X. Yang, H. Gao, X. Wang, I. Hussain and B. Tan, *Angew. Chem., Int. Ed.*, 2024, **64**, e202416350.
13 M. Liu, Q. Huang, S. Wang, Z. Li, B. Li, S. Jin and B. Tan, *Angew. Chem., Int. Ed.*, 2018, **57**, 11968–11972.
14 Y. Zhao, Y. Wang, W. Xue, R. Cheng, X. Zheng, G. Zhu, D. Hu, H. Huang, C. Hu and D. Liu, *Adv. Mater.*, 2024, **36**, 2403097.
15 M. Liu, K. Jiang, X. Ding, S. Wang, C. Zhang, J. Liu, Z. Zhan, G. Cheng, B. Li, H. Chen, S. Jin and B. Tan, *Adv. Mater.*, 2019, **31**, e1807865.
16 L. Guan, Z. Guo, Q. Zhou, J. Zhang, C. Cheng, S. Wang, X. Zhu, S. Dai and S. Jin, *Nat. Commun.*, 2023, **14**, 8114.
17 Z. Lei, M. Liu, Y. Zhang, L. Li, S.-Q. Zang and Z. Zheng, *Coord. Chem. Rev.*, 2025, **537**, 216703.
18 K. Kamiya, R. Kamai, K. Hashimoto and S. Nakanishi, *Nat. Commun.*, 2014, **5**, 5040.
19 M. Liu, W. H. Deng, X. Wang, J. Liu, S. Jin, G. Xu and B. Tan, *ChemSusChem*, 2022, **15**, e202201298.
20 N. Wang, G. Cheng, L. Guo, B. Tan and S. Jin, *Adv. Funct. Mater.*, 2019, **29**, 1904781.
21 S. Abednatanzi, P. Gohari Derakhshandeh, K. Leus, H. Vrielinck, F. Callens, J. Schmidt, A. Savateev and P. Van Der Voort, *Sci. Adv.*, 2020, **6**, eaaz2310.
22 X. Hu, Z. Zhan, J. Zhang, I. Hussain and B. Tan, *Nat. Commun.*, 2021, **12**, 6596.
23 Z. A. Lan, M. Wu, Z. Fang, Y. Zhang, X. Chen, G. Zhang and X. Wang, *Angew. Chem., Int. Ed.*, 2022, **61**, e202201482.
24 R. Zhuang, X. Zhang, C. Qu, X. Xu, J. Yang, Q. Ye, Z. Liu, S. Kaskel, F. Xu and H. Wang, *Sci. Adv.*, 2023, **9**, eadh8060.
25 T. Zhou, Y. Zhao, J. W. Choi and A. Coskun, *Angew. Chem., Int. Ed.*, 2019, **58**, 16795–16799.
26 J. Liu, P. Lyu, Y. Zhang, P. Nachtigall and Y. Xu, *Adv. Mater.*, 2018, **30**, 1705401.
27 Y. Li, S. Zheng, X. Liu, P. Li, L. Sun, R. Yang, S. Wang, Z. S. Wu, X. Bao and W. Q. Deng, *Angew. Chem., Int. Ed.*, 2018, **57**, 7992–7996.
28 L. Huo, M. Lv, M. Li, X. Ni, J. Guan, J. Liu, S. Mei, Y. Yang, M. Zhu, Q. Feng, P. Geng, J. Hou, N. Huang, W. Liu, X. Y. Kong, Y. Zheng and L. Ye, *Adv. Mater.*, 2024, **36**, 2312868.
29 P. Kuhn, M. Antonietti and A. Thomas, *Angew. Chem., Int. Ed.*, 2008, **47**, 3450–3453.
30 M. J. Bojdys, J. Jeromenok, A. Thomas and M. Antonietti, *Adv. Mater.*, 2010, **22**, 2202–2205.
31 X. Suo, F. Zhang, Z. Yang, H. Chen, T. Wang, Z. Wang, T. Kobayashi, C. L. Do-Thanh, D. Maltsev, Z. Liu and S. Dai, *Angew. Chem., Int. Ed.*, 2021, **60**, 25688–25694.
32 X. Zhu, C. Tian, S. M. Mahurin, S. H. Chai, C. Wang, S. Brown, G. M. Veith, H. Luo, H. Liu and S. Dai, *J. Am. Chem. Soc.*, 2012, **134**, 10478–10484.

33 S. Ren, M. J. Bojdys, R. Dawson, A. Laybourn, Y. Z. Khimyak, D. J. Adams and A. I. Cooper, *Adv. Mater.*, 2012, **24**, 2357–2361.
34 Z. Yang, H. Chen, S. Wang, W. Guo, T. Wang, X. Suo, D. E. Jiang, X. Zhu, I. Popovs and S. Dai, *J. Am. Chem. Soc.*, 2020, **142**, 6856–6860.
35 S. Y. Yu, J. Mahmood, H. J. Noh, J. M. Seo, S. M. Jung, S. H. Shin, Y. K. Im, I. Y. Jeon and J. B. Baek, *Angew. Chem., Int. Ed.*, 2018, **57**, 8438–8442.
36 T. Sun, Y. Liang, W. Luo, L. Zhang, X. Cao and Y. Xu, *Angew. Chem., Int. Ed.*, 2022, **61**, e202203327.
37 Y. Zou, S. Abednatanzi, P. Gohari Derakhshandeh, S. Mazzanti, C. M. Schusslbauer, D. Cruz, P. Van Der Voort, J. W. Shi, M. Antonietti, D. M. Guldi and A. Savateev, *Nat. Commun.*, 2022, **13**, 2171.
38 K. Wang, L. M. Yang, X. Wang, L. Guo, G. Cheng, C. Zhang, S. Jin, B. Tan and A. Cooper, *Angew. Chem., Int. Ed.*, 2017, **56**, 14149–14153.
39 M. Liu, L. Guo, S. Jin and B. Tan, *J. Mater. Chem. A*, 2019, **7**, 5153–5172.
40 H. Jiang, Z. Guo, H. Wang, X. Liu, Y. Ren, T. Huang, J. Xue, H. Wu, J. Zhang, Y. Yin, Z. Jiang and M. D. Guiver, *J. Membr. Sci.*, 2021, **640**, 119803.
41 Y. Zhu, M. Qiao, W. Peng, Y. Li, G. Zhang, F. Zhang, Y. Li and X. Fan, *J. Mater. Chem. A*, 2017, **5**, 9272–9278.
42 C. Wang, H. Zhang, W. Luo, T. Sun and Y. Xu, *Angew. Chem., Int. Ed.*, 2021, **60**, 25381–25390.
43 M. Liu, Z. Li, G. Wei, E. Fan, Q. Feng, D. Zhao, Y. Guo, Y. Zhang and Z. Zheng, *Cryst. Growth Des.*, 2023, **23**, 3349–3356.
44 R. Guo, J. Xia, H. Gu, X. Chu, Y. Zhao, X. Meng, Z. Wu, J. Li, Y. Duan, Z. Li, Z. Wen, S. Chen, Y. Cai, C. Liang, Y. Shen, G. Xing, W. Zhang and G. Shao, *J. Mater. Chem. A*, 2023, **11**, 408–418.
45 Y. Yang, H. Chen, C. Liu, J. Xu, C. Huang, C. D. Malliakas, H. Wan, A. S. R. Bati, Z. Wang, R. P. Reynolds, I. W. Gilley, S. Kitade, T. E. Wiggins, S. Zeiske, S. Suragtkhuu, M. Batmunkh, L. X. Chen, B. Chen, M. G. Kanatzidis and E. H. Sargent, *Science*, 2024, **386**, 898–902.
46 J. Zhang, X. Peng, H. Wu, G. Zhang, Y. Chen, W. Cai, Z. Pan, H. Rao and X. Zhong, *Angew. Chem., Int. Ed.*, 2025, **64**, e202423655.
47 Y. Zhang, Y. Liu, Z. Zhao, T. Kong, W. Chen, W. Liu, Y. Rong and D. Bi, *Adv. Mater.*, 2025, **37**, 2500501.
48 Y. Zhu, J. Zhang, H. Su, P. Wang, Y. She, X. Zheng, X. Liu, J. Wu, R. Wang, Y. Wang, D. Li and S. F. Liu, *Angew. Chem., Int. Ed.*, 2025, **64**, e202421637.
49 Y.-H. Lin, Vikram, F. Yang, X.-L. Cao, A. Dasgupta, R. D. J. Oliver, A. M. Ulatowski, M. M. McCarthy, X. Shen, Q. Yuan, M. G. Christoforo, F. S. Y. Yeung, M. B. Johnston, N. K. Noel, L. M. Herz, M. S. Islam and H. J. Snaith, *Science*, 2024, **384**, 767–775.
50 L. Zhang, T. Sun, Z. Zhang, Z. Zhang and Y. Xu, *Angew. Chem., Int. Ed.*, 2025, **64**, e202421251.
51 M. Liu, K. Yang, Z. Li, E. Fan, H. Fu, L. Zhang, Y. Zhang and Z. Zheng, *Chem. Commun.*, 2022, **58**, 92–95.
52 X. Wang, M. Liu, X. Wang and B. Tan, *Chem. Commun.*, 2022, **58**, 12313–12316.
53 P. Wu, J. Lu, F. Xi, X. Li, W. Ma, F. Kang, S. Li, Z. Tong and Q. Zhang, *Chem. Sci.*, 2025, **16**, 4127–4135.
54 S. Zhang, G. Cheng, L. Guo, N. Wang, B. Tan and S. Jin, *Angew. Chem., Int. Ed.*, 2020, **59**, 6007–6014.
55 J. Zhu, Y. Liu, B. He, W. Zhang, L. Cui, S. Wang, H. Chen, Y. Duan and Q. Tang, *Chem. Eng. J.*, 2022, **428**, 131950.
56 J. Zhu, B. He, W. Zhang, R. Tui, H. Chen, Y. Duan, H. Huang, J. Duan and Q. Tang, *Adv. Funct. Mater.*, 2022, **32**, 2206838.
57 J. Zhu, B. He, X. Yao, H. Chen, Y. Duan, J. Duan and Q. Tang, *Small*, 2022, **18**, e2106323.
58 B. Zhang, Y. Lei, R. Qi, H. Yu, X. Yang, T. Cai and Z. Zheng, *Sci. China Mater.*, 2018, **62**, 519–526.
59 E. Fan, M. Liu, K. Yang, S. Jiang, B. Li, D. Zhao, Y. Guo, Y. Zhang, P. Zhang, C. Zuo, L. Ding and Z. Zheng, *Nano-Micro Lett.*, 2023, **15**, 58.
60 J. Yang, J. Fu, W. Dong, S. Ren, X. Zhang, J. Su, C. Zhao, M. Wei, D. Zhao, Y. Zhang, S. Wu and Z. Zheng, *Energy Environ. Sci.*, 2024, **17**, 9346–9358.
61 Y. Lei, L. Gu, W. He, Z. Jia, X. Yang, H. Jia and Z. Zheng, *J. Mater. Chem. A*, 2016, **4**, 5474–5481.
62 E. C. Fan, M. Y. Liu, Y. G. Zhang, D. D. Zhao, Y. Lei, C. L. Zhao, P. Zhang, E. J. Zhou and Z. Zheng, *Infomat*, 2025, **7**, e700.